Journal of Power Sources 245 (2014) 208–216

Contents lists available at SciVerse ScienceDirect

Journal of Power Sources

journal homepage: www.elsevier.com/locate/jpowsour

Physical characterization of the charging process of a Li-ion battery and prediction of Li plating by electrochemical modelling

N. Legrand [a,b,c,*], B. Knosp [a], P. Desprez [a], F. Lapicque [b], S. Raël [c]

[a] SAFT, Direction de la Recherche, 111/113 boulevard Alfred Daney, 33074 Bordeaux Cedex, France
[b] LRGP, CNRS – Université de Lorraine, BP 20451, 54001 Nancy, France
[c] Université de Lorraine, GREEN, 54518 Vandoeuvre-lès-Nancy, France

HIGHLIGHTS

- We present a new method to access the charging process of a Li-ion battery.
- We investigate the Li plating through charge transfer limitation.
- We take advantage of an electrochemical model to characterize the Li plating.
- Abacuses are set up from modelling of charge pulse solicitations.
- An experimental validation of the method is performed on a VL41M SAFT cell.

ARTICLE INFO

Article history:
Received 29 April 2013
Received in revised form
17 June 2013
Accepted 21 June 2013
Available online 29 June 2013

Keywords:
Lithium-ion battery
Charging
High rate
Charge transfer
Li plating
Electrochemical modelling

ABSTRACT

This paper deals with occurrence of lithium plating on the negative electrode of lithium-ion batteries, a significant ageing phenomenon known to damage lithium-ion battery performances.

Charge transfer process, one of the two different steps of the process of Li insertion in the negative active material being the cause of this ageing, was considered here to be the limiting process. This transfer occurs at short-time scales. The second process, the diffusion of lithium in the solid insertion compound, occurring at relatively long-time scales, has not been fully examined here.

The aim of this paper was to develop a new method to evaluate the maximal rate of a charge pulse solicitation to prevent this ageing phenomenon. The approach relies on the use of a fundamental model of lithium ion battery with coupled mass and charge transfer. To validate the method, 2 s microcycles have been performed on a commercial VL41M SAFT cell. Theoretical and experimental works led to the maximum current density to be applied without undesired Li deposition, depending on the state of charge (SOC). The abacus established for the cell of interest can orient further specifications for suitable use of the battery.

1. Introduction

Nowadays, lithium-ion (Li-ion) batteries are used in numerous applications from stationary to transportation applications. With special concern to transport application, the world request is becoming more and more important. This rise is due to a large extent to the future emergence of hybrid and electric vehicles.

As regard to the application requests Li-ion batteries need to exhibit a long service life. However according to the operating cycling and storage conditions its initial performances are degraded along operating time [1–4]. Because of this appreciable decrease, ageing actually represents a significant matter of concern. In this context, numerous studies [5–8] have been carried out with the view to better understanding the origin of ageing mechanisms depending on electrode chemistry.

Concerning the negative electrode, it is pointed out that ageing with operating time could be caused by the volume changes during cycling, decomposition of the binder, current collector corrosion, and finally by metallic lithium plating and subsequent solid electrolyte interface (SEI) growth [5–7]. For positive electrode concern, various ageing sources can be mentioned: volume changes during cycling – although less dramatic than in the negative electrode – , dissolution of the active material in the electrolyte, current

* Corresponding author. SAFT, Direction de la Recherche, 111/113 boulevard Alfred Daney, 33074 Bordeaux Cedex, France. Tel.: +33 557 10 94 85; fax: +33 557 10 68 77.
E-mail address: nathalie.legrand@saftbatteries.com (N. Legrand).

0378-7753/$ – see front matter © 2013 Elsevier B.V. All rights reserved.
http://dx.doi.org/10.1016/j.jpowsour.2013.06.130

collector corrosion, alteration of active particle surface, electrolyte decomposition and surface layer formation [5,8]. With concern to the separator, formation and growth of the SEI can result in clogging of the pore network [5] after long operations, resulting in porosity decrease. This list of possible ageing mechanisms is not exhaustive. Nevertheless, the ageing phenomenon usually considered as the most detrimental in normal use conditions is occurrence of the SEI growth. This particular growth can be exacerbated by Li plating on the negative electrode [9,10].

Obviously interaction of the above ageing mechanisms can occur and single ageing mechanisms may be difficult to isolate. Nevertheless for the sake of simplicity we consider in this paper one mechanism appearing to be of prime importance for Li-ion battery, namely Li plating. Indeed, the plated Li induces a significant increase of frozen lithium in the SEI and obviously electrode capacity mismatching (Fig. 1).

The effects of this ageing are not observed during shelf storage but during cycling – regular – operation and occur at the surface of the negative active particles. Lithium plating occurs in charge conditions and particularly in case of fast charging. It can be promoted by two specific cycling conditions: charge at high currents or at low temperatures. Li plating can originate from two different processes: the charge transfer and the lithium solid diffusion (Fig. 2). On the one hand, the charge transfer overvoltage appears as soon as the current is applied. As a consequence, this process, hereafter named as charge transfer limitation (CTL), can be rate-limiting for sufficiently high charge currents and whatever the initial state of charge. These conditions may be fulfilled, for instance, for energy recovery of a regenerative brake or load levelling of the energy hybrid sources [11,12]. On the other hand, for lower charge rates i.e. outside the charge transfer limitation case, but for which sufficiently large concentration gradients can exist due to the Li solid diffusion, the particle surface can become saturated. This limitation – called hereafter SDL for solid diffusion limitation – is promoted by high initial states of charge.

Very few investigations have been reported in the relevant literature to establish the suitable domains of operating conditions to avoid this kind of ageing phenomena in Li-ion batteries. For instance, Zhang et al. [9,10] designed three-electrode Li-ion cells with metal lithium as the reference electrode to investigate the occurrence of Li plating and to search for appropriate charging protocols. Arora and al. used a model to optimize the cell design against Li plating [13]. Perkins and al. developed a reduced model of Li plating and compared it with a fundamental model implemented under COMSOL software without experimental validations [14]. On the contrary, the present study was aimed at evaluating the risk of Li plating caused by charge transfer limitation as a function of the charge rate of commercial Li-ion cells.

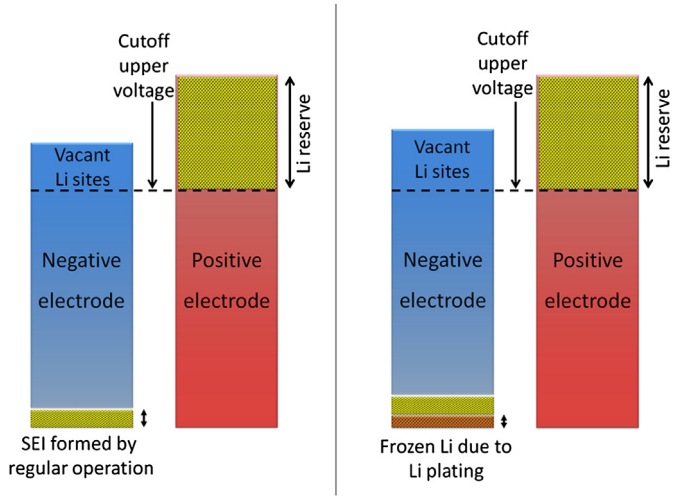

Fig. 1. Illustration of electrode capacities before (left) and after (right) ageing by Li plating.

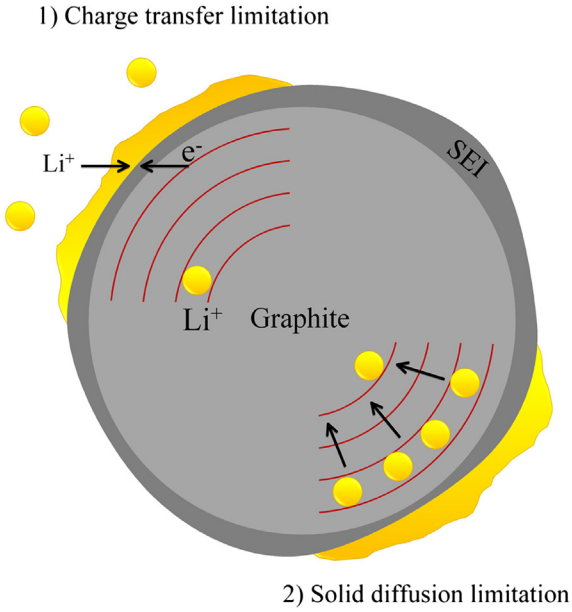

Fig. 2. Schematic illustration of Li plating occurring at the surface of the negative active particle: 1) from charge transfer limitation and 2) from solid diffusion limitation.

For this purpose the Li-ion model developed by Smith and Wang [15] and relying upon the pioneering Newman's contributions [16–19] in the area has been used: charge and mass transport phenomena in porous electrodes have been considered, using the transport formalism for concentrated solutions. Experiments were carried out with SAFT commercial batteries operated in short-time cycling, allowing validation of the model for prediction of Li plating occurrence.

2. The Li plating

At high charge rates for which Li plating occurs, the two following reactions coexist [9]:

$$x\mathrm{Li}^{+} + \mathrm{Li}_{\delta}\mathrm{C}_6 + x\mathrm{e}^{-} \rightarrow \mathrm{Li}_{\delta+x}\mathrm{C}_6 \quad (1)$$

$$(1-x)\mathrm{Li}^{+} + (1-x)\mathrm{e}^{-} \rightarrow (1-x)\mathrm{Li}^{\circ} \quad (2)$$

Then, independently of the presence of any external current, two subsequent reactions can occur:

$$\varepsilon\mathrm{Li}^{\circ} + \mathrm{Li}_{\delta+x}\mathrm{C}_6 \rightarrow \mathrm{Li}_{\delta+x+\varepsilon}\mathrm{C}_6 \quad (3)$$

$$\mathrm{R} + \mathrm{Li}^{\circ} \rightarrow \mathrm{R}-\mathrm{Li} \quad (4)$$

Reaction (1) is the insertion reaction and reaction (2) corresponds to the lithium deposition. A subsequent reaction (3) between plated lithium and not-saturated graphite can take place. Another subsequent reaction (4) is the reduction of the carbonate solvent electrolyte R by the plated lithium to form an additional SEI [8]. This new SEI is also believed to isolate Li metal grains which become inactive. Indeed, this new SEI has to be distinguished from

the required original SEI, formed during the first cycles to protect the graphite electrode (Fig. 1).

The fractional occupancy – or stoichiometry coefficient of the lithium guest species – will be designated by x_{neg} in the following to avoid confusion with coordinate x, perpendicular to the electrode surface in the model.

As mentioned before, the Li plating is the result of two different limitation kinds: CTL and SDL. Moreover, the plating can be promoted by particular charge conditions and low temperatures. As a matter of fact, low temperatures slow down the kinetic mechanisms, like charge transfer and lithium solid state diffusion [1].

Li plating can thermodynamically occur locally as soon as the negative electrode potential E_{neg} becomes lower than or equal to the equilibrium potential E_{Li^+/Li° of reaction (2):

$$E_{neg} \leq E_{Li^+/Li^\circ} \tag{5}$$

i.e. as soon as the overpotential absolute value $|\eta_{neg}|$ exceeds the overpotential limit: $|\eta_{lim}|$ (Fig. 3), at the negative electrode. Eq. (5) can be written as:

$$E_{neg,eq} + \eta_{neg} \leq E_{Li^+/Li^\circ,eq} + \eta_{Li^+/Li^\circ}$$

which yields:

$$OCV_{neg}(x_{neg}) + \frac{RT}{F}\ln(a_{Li^+}) + \eta_{neg} \leq E^\circ_{Li^+/Li^\circ} + \frac{RT}{F}\ln x(a_{Li^+}) + \eta_{Li^+/Li^\circ}$$

Since η_{neg} and η_{Li^+/Li° are negative during the charge, the above equation leads to:

$$|\eta_{neg}| \geq |\eta_{lim}| = OCV_{neg}(x_{neg}) - E^\circ_{Li^+/Li^\circ} + |\eta_{Li^+/Li^\circ}| \tag{6}$$

with $E_{neg,eq}$ and $E_{Li^+/Li^\circ,eq}$ the equilibrium potentials of reaction (1) and (2) respectively, η_{Li^+/Li° the overpotential of the reaction (2), $OCV_{neg}(x_{neg}) = E^\circ_{neg} + f(x_{neg})$ the open circuit voltage of the negative electrode (V vs Li^+/Li°), E°_{neg} and $E^\circ_{Li^+/Li^\circ}$ the standard potentials of each reaction (V), f a function of x_{neg}, R the gas constant (J mol^{-1} K^{-1}), F the Faraday constant (C.eq^{-1}), T the temperature (K) and a_{Li^+} the Li^+ activity.

2.1. The charge transfer limitation: CTL

As shown by Fig. 3, occurrence of Li plating is favoured because the lithium insertion inside graphite occurs within a narrow potential range ([65–200] mV vs. Li^+/Li°) close to the thermodynamic potential of the Li^+/Li° couple, especially at high insertion level ($x_{neg} \approx 1$ in $Li_{x_{neg}}C_6$). Indeed, insertion and extraction of lithium occur within a narrow potential range through multiple phase transitions. In particular, the last phase transition from LiC_{12} to LiC_6 is observed at a potential plateau around 65 mV vs. Li^+/Li°.

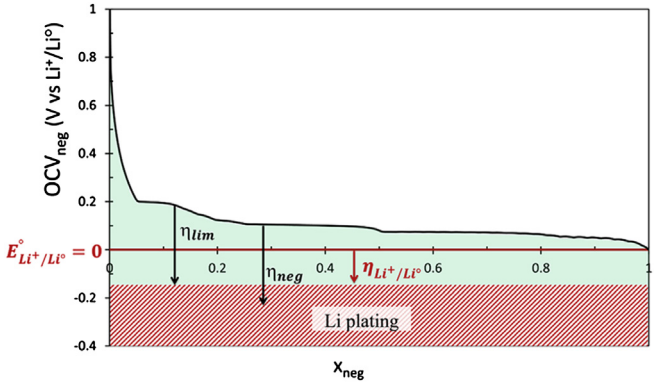

Fig. 3. Schematic representation of Li plating occurrence.

Verbrugge and Koch [20] experimentally demonstrated that graphite can tolerate, i.e. without Li plating occurrence, moderately negative potentials (200 mV relative to the lithium reference) for brief periods of time.

Nevertheless, the kinetics of metal lithium electroplating on the carbon electrode is not known precisely and depends mainly on the nature of the carbonaceous electrode. As a consequence, we considered that Li plating can occur as soon as the thermodynamic condition $|\eta_{Li^+/Li^\circ}| \geq 0$ is fulfilled, i.e. when $|\eta_{neg}|$ exceeds $|\eta_{lim}| = OCV_{neg}(x_{neg}) - E^\circ_{Li^+/Li^\circ}$ (Fig. 3).

It is considered here that the charge transfer of the insertion reaction follows locally a Butler–Volmer kinetic law:

$$j_{BV} = a_s j_0 \left\{ \exp\left(\frac{\alpha_o F}{RT}\eta\right) - \exp\left(-\frac{\alpha_r F}{RT}\eta\right) \right\} \tag{7}$$

with a_s the specific interfacial area of active particles (m^2 m^{-3}), j_0 the exchange current density (A m^{-2}), α_o and α_r the oxidation and reduction transfer coefficients and η the overpotential (V).

From the above Butler–Volmer equation and the relationship between η_{lim} and the state of charge – using for instance the numerical law of the OCV proposed by Smith and Wang [15,21,22] – the theoretical maximal acceptable current density $|j_{BV,lim} \cdot a_s^{-1}|$ can be computed by assuming a uniform current distribution across the electrode.

This kind of limitation takes place instantaneously, delayed by the double layer capacitance time constant, which is of a few µs [16].

2.2. The solid lithium diffusion limitation: SDL

In the active particle, the inserted lithium moves by diffusion according to Fick's law involving the Li concentration in the solid phase calculated on the basis of number of available sites. A solid diffusion coefficient characterizes this mass transport, whose dependence on temperature follows an Arrhenius-type law:

$$D_s = C\exp\left(-\frac{E_a}{RT}\right) \tag{8}$$

where C is a constant (m^2 s^{-1}) and E_a is the activation energy for the diffusion process (J mol^{-1})

Fig. 4 shows schematically the lithium concentration profile in the particle. It depends on the diffusion coefficient and the charge rate. When the matrix close to the surface becomes saturated – the local concentration c_s reaches the maximal concentration $c_{s,max}$ – only a part of the lithium can be absorbed by the compound. The current excess induces Li plating.

Contrary to CTL, SDL can take place at relatively long-time scales as regard to the characteristic diffusion time τ_D [21], calculated with Smith and Wang's data set [15,21,22]:

$$\tau_D = \frac{R^2_{s,neg}}{D_{s,neg}} \approx 5000 \text{ s} \tag{9}$$

This characteristic time can be related to continue charge solicitations. This second limitation kind will be investigated in a further work.

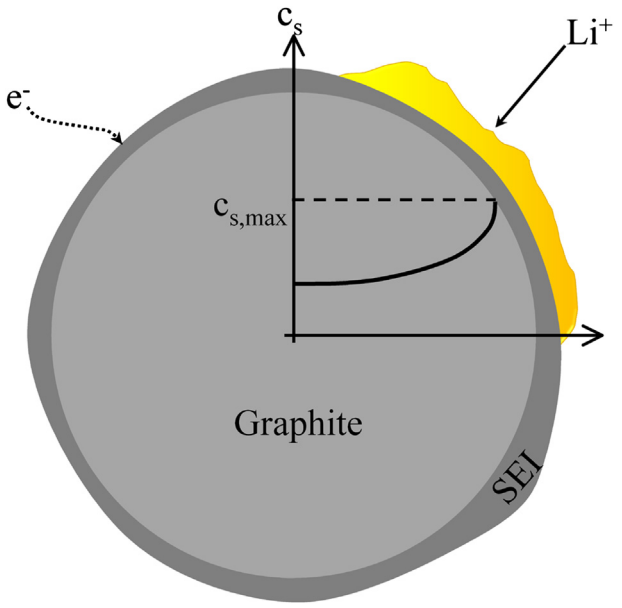

Fig. 4. Inserted Li concentration profile with surface saturation.

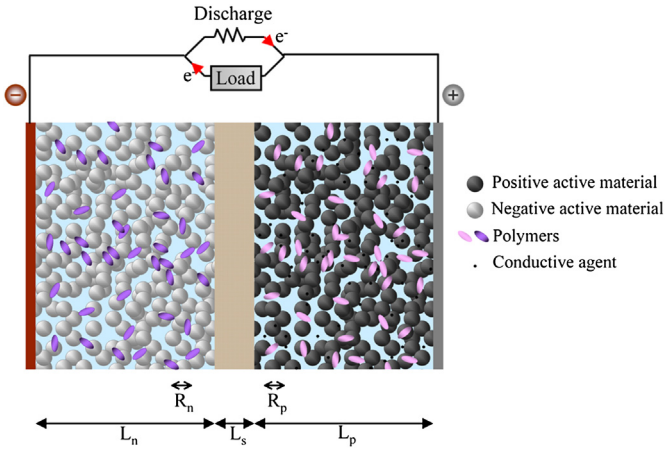

Fig. 6. Schematic representation of the three main regions in Li-ion cell.

2.3. Summary

Four different cases can be identified depending on the charge current (Fig. 5). In the first case, no Li plating should be detected. Following cases refer to situations where Li plating can thermodynamically occur (dashed zones). Case 2 represents Li plating from charge transfer limitation. Case 4 is associated to Li plating from solid lithium diffusion limitation. Case 3 refers to Li plating from mixed limitations.

3. Model implementation

The model implemented in COMSOL Multiphysics V4.3.0.184 is a double 1-D model based on physical and electrochemical processes of a Li-ion cell, derived from the insertion-type porous electrode and concentrated solution theories resulting from Newman's works [16]. The governing equations of the electrochemical system are not completely detailed here since most of them have been developed in previous studies [15–19,21–24].

As shown in Fig. 6, the Li-ion battery consists in three main regions: the negative electrode, the separator and the positive electrode. The model is implemented here for $Li_{x_{neg}}C_6$ negative electrode and $Li_{x_{pos}}Ni_{1-y-z}Co_yAl_zO_2$ positive electrode chemistry (x_{neg} and x_{pos} are the solid phase lithium stoichiometry) in which the liquid electrolyte is composed of a single $LiPF_6$ salt dissolved in an organic mixture of linear or cyclic carbonate solvents such as ethylene carbonate (EC), propylene carbonate (PC) and dimethyl carbonate (DMC).

The negative and positive electrode domains are composed of two media: (i) a solid mixture of the solid active insertion particles blended with an inert polymer and a suitable conducting agent, and (ii) the liquid electrolytic contained in the pores. As a result, the electrode domains have been modelled as the superimposition of

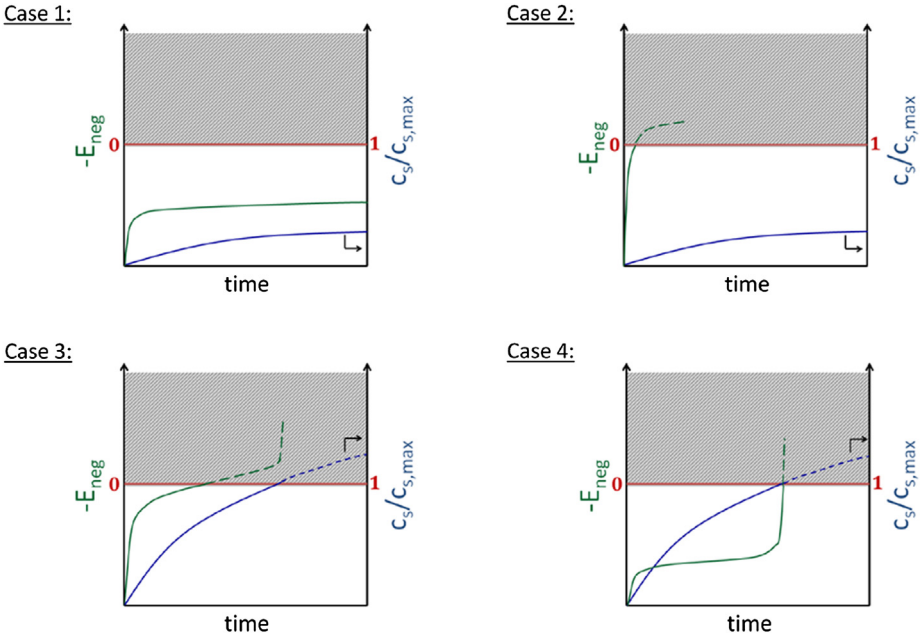

Fig. 5. Illustrations of the different cases encountered during a charge solicitation. (1) no Li plating; (2) Li plating from CTL; (3) Li plating from CTL and SDL; (4) Li plating from SDL.

the continuous solid and the solution media (Fig. 6) by using a conventional model with l and r coordinates, respectively perpendicular to the electrode surface and to the surface particle [24]. Finite element method was used; each domain was discretized in 40 elements. It can be noticed that the model has been written dimensionless with reduced coordinates x and y, corresponding respectively to l and r, and the current collectors were not accounted for in the representation since their electronic conductivity was assumed to be infinite.

Each media has been described by its own volume fraction. Concerning the separator section, it is physically made of a pore network, characterized by its porosity ε_e and its tortuosity τ. The two features are related by a Bruggeman-type relation [25] with coefficient β:

$$\tau = \varepsilon_e^{1-\beta} \tag{10}$$

The solid active material particles were assumed to be monodisperse spheres in each electrode. The volume variation during charge or discharge was considered here to be negligible. As a consequence the porosity was kept as a constant value. Moreover parameter a_s representing the specific surface area of the electrochemical interface per electrode volume unit is simply expressed as follows:

$$a_s = \frac{3\varepsilon_s}{R_s} \tag{11}$$

where ε_s is the volume fraction of the active material in the electrode and R_s the radius of the active particles. The SEI layer was not taken into account in this work. The model does not either take into account heat transfer phenomena occurring in the battery but physical parameters were defined and calculated depending on the temperature.

The different physical processes taken into account in the model were the following: migration and diffusion of ions in the electrolytic phase, diffusion of inserted lithium in solid active particles, and electric conduction of both ions and electrons in the electrolytic and solid media respectively. Convection was neglected in the model. Four variables were therefore involved in the model equations: (i) the concentration of salt ions, $c_e(x,t)$, (ii) the concentration of inserted lithium in the active solid material, $c_s(r,t)$, (iii) the potential in the solid active material phase, $\Phi_s(x,t)$ and (iv) the potential in the solution, $\Phi_e(x,t)$.

Therefore the model relies on coupled differential equations established and used in previous investigations [15–19,21–24]: the equations summarized in Table 1 are related to charge transport – for e^-, $Li^+$and PF_6^- – and mass transport – for Li, Li^+ and PF_6^-. The kinetics of electrochemical processes are assumed to obey Butler–Volmer laws (Eq. (7)).

4. Model methodology for determination of the maximal acceptable current

The deposition reaction is considered thermodynamically possible when the absolute value of the electrode overpotential $\left|\eta_{neg}\right|$ becomes larger than the electrode equilibrium potential vs. Li^+/Li°: OCV_{neg}. With the model variables used here, the reaction is thermodynamically possible when:

$$\Phi_s - \Phi_e < 0 \tag{12}$$

Investigation on possible occurrence of the deposition was led in transient conditions, by considering different pulses of current. As explained above, short periods of time have to be considered here. Operations with a current pulse could be simulated by using the above model for different considered time periods. These simulations allow to check whether Eq. (12) is fulfilled during the charge. Fig. 7a. shows an example of the time variations of E_{neg} calculated at three different locations of the negative surface. The point at the negative separator interface ($x = 1, y = 1$) appears to be the critical location for simulations which is linked to the relative conduction of the electrode and electrolyte phases and has been considered for further predictions of onset of Li plating.

Further, for each considered pulse duration, successive simulations have been run by increasing the charge current to determine the critical current density whereby onset of Li plating occurs exactly at the end of the pulse, as exemplified in Fig. 7b. This critical C rate is obtained for various initial SOCs corresponding to given initial x_{neg} values. The results obtained with the Smith and Wang's data set of parameters [15,21,22] have been gathered in the form of an abacus, as shown in Fig. 8: Li deposition in CTL at 1 ms occurs at very high current densities (~25 A m^{-2} on the basis of active material surface area). For this time range, the double layer

Table 1
Governing equations.

$\forall t$	Conservation equations (mol m^{-3} s^{-1} or A m^{-3})	Boundary conditions (mol m^{-2} s^{-1} or A m^{-2})
Species, electrolytic phase	$\varepsilon_e\frac{\partial c_e}{\partial t} = \frac{\partial}{\partial l}\left(D_e^{eff}\frac{\partial c_e}{\partial l}\right) + \frac{1-t_p}{F}j_{BV}$	$\frac{\partial c_e}{\partial l}\Big\vert_{l=0,L_n+L_s+L_p} = 0$
Species, active material	$\frac{\partial c_s}{\partial t} = \frac{1}{r^2}\frac{\partial}{\partial r}\left(D_s r^2\frac{\partial c_s}{\partial r}\right)$	$-D_s\frac{\partial c_{s,l}}{\partial r}\Big\vert_{r=Rs} = \frac{j_{BV}}{a_s F}$; $\frac{\partial c_s}{\partial r}\Big\vert_{r=0} = 0$
Charge, electrolytic phase	$\left\{\frac{\partial}{\partial l}\left(\frac{2RT\kappa_e^{eff}}{F}(t_p-1)\left(1+\frac{d\ln f_{\pm}}{d\ln c_e}\right)\frac{\partial \ln c_e}{\partial l} + \kappa_e^{eff}\frac{\partial \Phi_e}{\partial l}\right) + j_{BV} = 0\right.$	$\frac{\partial \Phi_e}{\partial l}\Big\vert_{l=0,L_n+L_s+L_p} = 0$
Charge, solid media	$\frac{\partial}{\partial l}\left(-(1-\varepsilon_e)\sigma_s\frac{\partial \Phi_s}{\partial l}\right) + j_{BV} = 0$	$\frac{\partial \Phi_s}{\partial l}\Big\vert_{l=L_n,L_n+L_s} = 0$; $-\varepsilon_s\sigma_s\frac{\partial \Phi_s}{\partial l}\Big\vert_{l=0,L_n+L_s+L_p} = J_{cell}$; $\Phi_s\vert_{l=0} = 0$

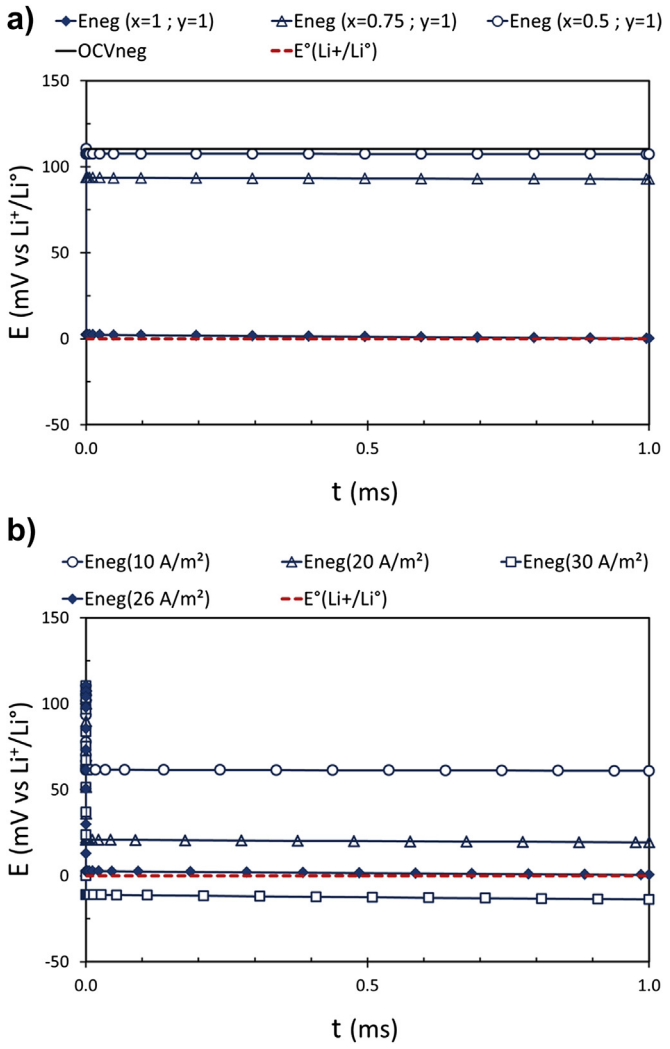

Fig. 7. Li plating limit condition shown in the form of the negative electrode potential: a) at three different locations in the negative electrode and its corresponding OCV curve for a 26 A m^{-2} current step during 1 ms pulse and b) at the negative separator interface during 1 ms pulse for four different currents, starting from 40% SOC at 25 °C, with Smith and Wang's data set [15,21,22].

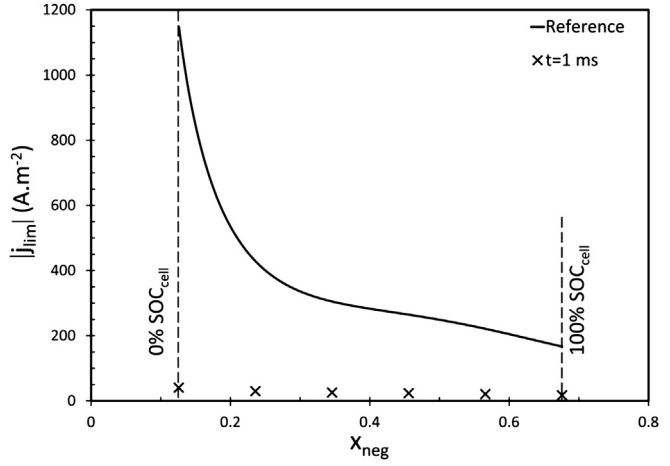

Fig. 8. Abacus of the maximal acceptable current per active material surface area to avoid Li plating due to charge transfer limitation after 1 ms pulse and "reference curve" using Smith and Wang's data set at 25 °C [15,21,22].

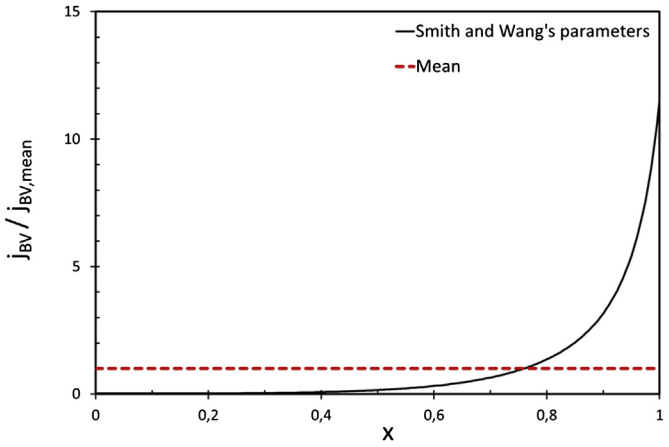

Fig. 9. Profile of the ratio of the local reaction current density over mean reaction current density for lithium insertion across the negative electrode thickness at $t = 1$ ms of a 26 A m^{-2} charge starting at 40% initial SOC and at 25 °C, using Smith and Wang's data set [15,21,22].

capacitance should have also been taken into account in the model. Nevertheless, presence of the capacitance would have only delayed the plating occurrence, without altering the conclusions drawn. The results obtained were compared to $\left|j_{\mathrm{BV,lim}} \cdot a_s^{-1}\right|$ (cf. Section 2.1.) called hereafter "reference curve" in Fig. 8.

This "reference curve" is orders of magnitude above the critical current density calculated for various pulse periods. As a matter of fact, the "reference curve" has been calculated assuming a uniform current density across the negative electrode. Simulations yielded the current density in the negative electrode volume: this distribution obtained is shown to be far from uniform as exemplified in Fig. 9 which gives the current density over the mean reaction current density for charging at 26.5 A m^{-2} starting from 40% SOC. For electrode conception purpose and to handle high charge rates, similar conductions in the electrolyte and in the active mass phases of the negative electrode have to be searched.

5. Experimental validation

5.1. Electrical tests

Dedicated experimental tests have been performed to validate the investigation methodology. For this part, VL41M type cells

Table 2
SAFT VL41M cell data sheet [26].

	VL41M
Electrical characteristics	
Nominal voltage (V)	3.6
Average capacity C/3 after charge to 4.0 V/cell (A h)	41
Minimum capacity C/3 after charge to 4.0 V/cell (A h)	39
Specific energy after charge to 4.0 V/cell (Wh kg^{-1})	136
Energy density after charge to 4.0 V/cell (Wh dm^{-3})	285
Specific power (30 s peak 50% DOD) (W kg^{-1})	794
Power density (30 s peak 50% DOD) (W dm^{-3})	1667
Mechanical characteristics	
Diameter (mm)	54.3
Height (mm)	222
Typical weight (kg)	1.07
Volume (dm^3)	0.51
Voltage limits	
Charge (V)	4.0 (4.1 for peak)
Discharge (V)	2.7 (2.3 for peak)
Current limits	
Maximal continuous current (A)	150
Maximal peak current during 30 s (A)	300

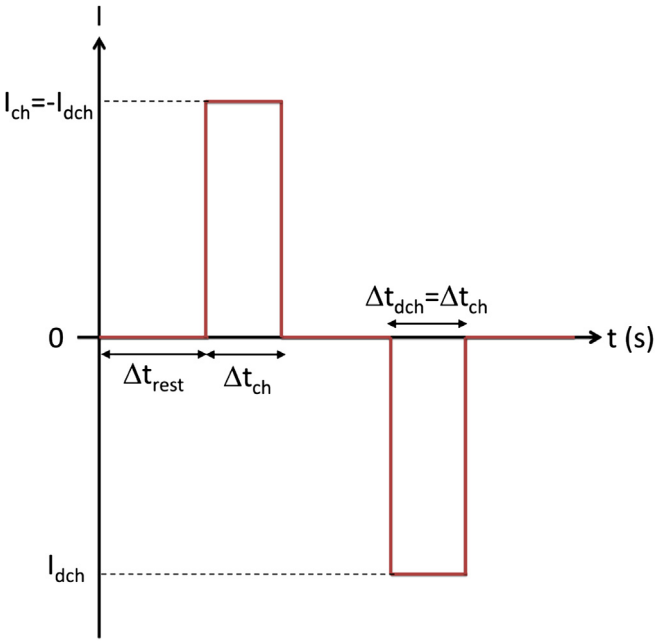

Fig. 10. Imposed current profile during the microcycles of the pulse solicitation at 25 °C.

produced by SAFT have been used. Table 2 reports the general characteristics of this battery type [26].

For the validation, VL41M production cells at a given initial cell SOC (100% SOC corresponds to 4 V and 0% SOC to 2.7 V) were submitted to short-period cycling – microcycles here – until a $20Q_{cell}$ cumulated charged capacity was reached (Q_{cell} is the rated capacity (A h)). The cycle profile used here is schematically presented in Fig. 10.

During this microcycle the time duration of the rest periods Δt_{rest} was fixed at 10 s and the time durations of the charge and discharge periods Δt_{ch} and Δt_{dch} respectively were of 2 s. These periods of time have been chosen to be as short as possible to avoid temperature increase and to be in charge transfer limitation only, taking into account the performance of the used electrical supply and controller (Digatron® MBT 500/200-050 S; discharge current range: [0.5 A–500 A] and voltage range: [0 V–20 V]). Moreover charge and discharge currents had the same intensity so that the SOC was considered as not affected by the microcycling operation. Steady state SOC on the active material surface is difficult to assess precisely and has been considered here as unchanged by the test.

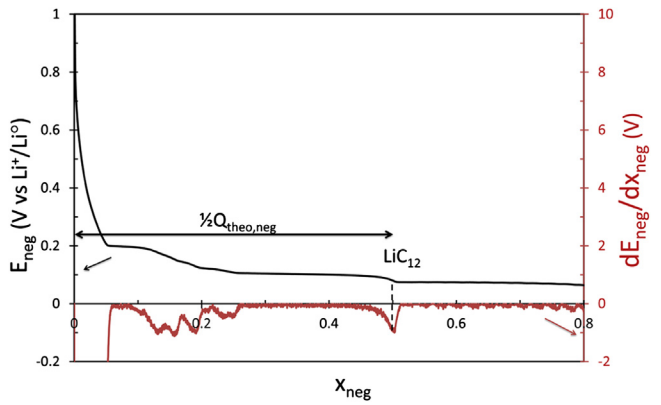

Fig. 11. Experimental variations of the graphite electrode potential vs. reference electrode and its zoomed derivative with respect to Li insertion rate in the negative electrode at *C*/50and 25 °C.

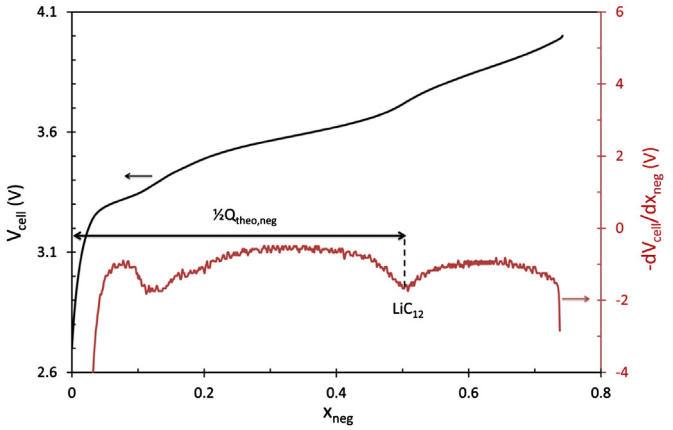

Fig. 12. Experimental variations of the VL41M cell voltage and its zoomed derivative with respect to Li insertion rate in the negative electrode at *C*/50and 25 °C.

Microcycling operation has been carried out for various initial SOCs and using several increasing charge currents: for this purpose, the cell was kept in a climatic chamber for the sake of constant temperature in spite of the appreciable heat evolved in particular at high currents.

In the example shown here, the tests were carried out for initial SOCs corresponding to x_{neg} near 0.5 and 0.6, for currents ranging from 2C to 12C i.e. from 80 to 500 A. The maximal charge current was evaluated by testing different currents and checking the capacity loss induced by the test. It is the case when the capacity loss during the cycle solicitation becomes of visible significance, i.e. above 0.5% capacity loss for $20Q_{cell}$ cumulated charged capacity.

5.2. Ageing characterization on the entire cell

After microcycling operation the cell was allowed to relaxation for 24 h. Capacity loss was then evaluated and the differential variation of the cell voltage along the charge – $dV_{cell}/dSOC$ – calculated and plotted versus SOC, as described in previous works [27]. This technique allows to detect the cell performance decay and to evaluate the degradation extent of the negative electrode. Concerning the negative electrode, it is known that the derivative function of the graphite electrode potential exhibits specific features corresponding to the different possible insertion stages

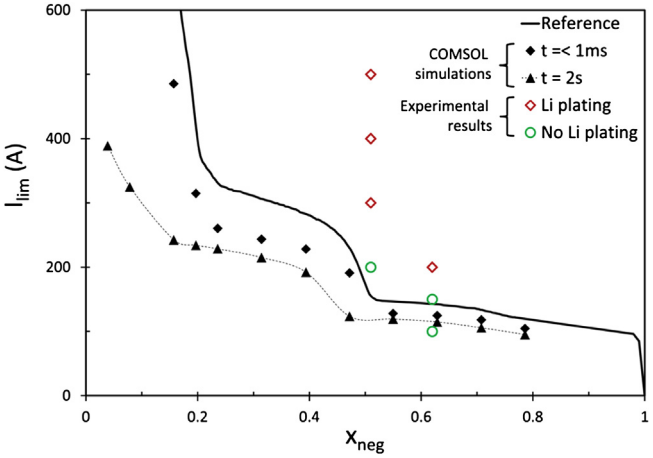

Fig. 13. Experimental results from a VL41M cell (open symbols) and abacus of the maximal acceptable current to avoid Li plating due to charge transfer limitation after different duration pulses and "reference curve" using VL41M cell parameters at 25 °C.

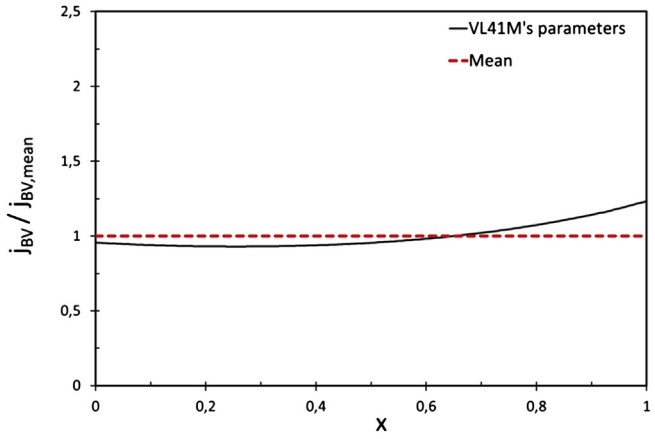

Fig. 14. Profile of the ratio of the local reaction current density over the mean reaction current density for VL41M's set of parameters across the negative electrode thickness after charging for 2 s at ~200 A and 25 °C starting from 40% initial SOC.

(Fig. 11). The LiC_{12} peak is particularly worth considering because it is well defined. Fig. 12 gives an example of differential cell voltage profile obtained with the VL41M SAFT cell. It reveals that the peaks of the negative graphite electrode – and more particularly the peak for LiC_{12} phase – can be identified also in complete cells.

After a cycle period a control discharge was performed at *C*/50 rate, which resulted in a negative limitation of the cell ($x_{0\%SOC,neg} \approx 0$). The distance between $x_{neg} = 0$ and $x_{neg} = 0.5$ was controlled to be unchanged. Any change in the distance would reveal deterioration of the carbon electrodes and consequently a loss of insertion sites. If this condition is fulfilled, reduction in x_{neg} (corresponding to 100% SOC) reveals a loss of cell capacity attributed to Li plating. Beyond 0.5% of capacity loss, it was considered that Li plating has occurred.

5.3. Results

The "reference curve" was computed and the COMSOL simulations were performed using the data set corresponding to the

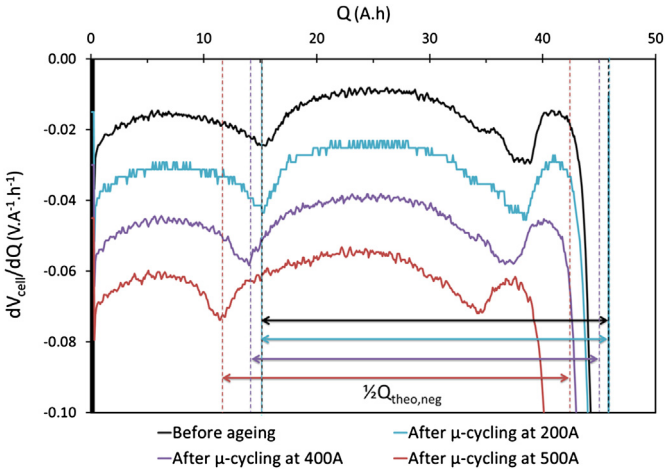

Fig. 15. Experimental variations of the zoomed derivative with respect to the discharged capacity at *C*/50and 25 °C before (black) and after ageing by microcycling at 200 A (blue), 400 A (purple), 500 A (red) for initial SOC corresponding to $x_{neg} \approx 0.5$. The translations along the capacity axis of the peaks correspond to the capacity variation due to Li plating. The translations along the ordinate axis are added for better clarity of the figure. (For interpretation of the references to colour in this figure legend, the reader is referred to the web version of this article.)

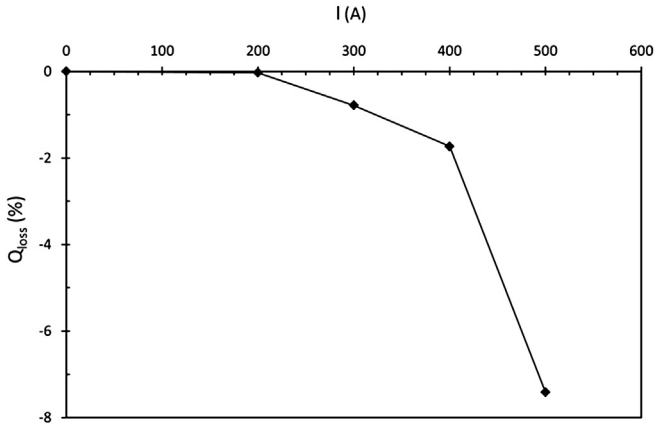

Fig. 16. Relative discharged capacity loss after microcycles for $20Q_{cell}$ cumulated charged capacity at different currents and for initial SOC corresponding to $x_{neg} \approx 0.5$.

VL41M cell. For industrial property reasons, intrinsic characteristics and performances of the cell are not shown here. The abacus for the VL41M cell, set up as previously explained, is shown in Fig. 13. It summarizes the results of numerous simulations performed for various charge currents starting from each of the 12 different considered initial states of charge and for two critical times. Additionally, it implies at least three trial charge currents per closed symbols in Fig. 13. It can be noticed that the smaller is the simulation pulse duration the closer to the instantaneous theoretical curve is the critical current.

The distance between simulation results and "reference curve" of Li plating occurrence for VL41M is lower than for Smith and Wang's data set. It is due to the difference in parameter data sets. Fig. 14 shows that the current distribution throughout the electrode is much more uniform for VL41M cell than this predicted by Smith and Wang's data set given in Fig. 9.

The experimental results of cycles for x_{neg} near 0.5 and 0.6 have also been reported in Fig. 13. As expected, it can be seen no Li plating has occurred for current range below the 2 s simulation limit (dotted line in Fig. 13) and also under the "reference curve".

In addition, Fig. 15 illustrates an example of derivative curves before and after ageing at different currents of microcycling for the initial SOC corresponding to $x_{neg} \approx 0.5$. The half theoretical negative capacity $½Q_{theo,neg}$, which is the distance between LiC_{12} peak and the end of the discharge limited thermodynamically by the negative electrode, is maintained. It means that the negative particle has not been deteriorated. As a result, the measured relative loss of discharged capacity Q_{loss} (Fig. 16) corresponds directly to the displacement of the LiC_{12} peak (Fig. 15). These observations confirm the origin of Li plating.

6. Conclusions

The Li plating ageing phenomenon has been studied under charge transfer limitation. This phenomenon occurs at a short-time scale. A method to evaluate the maximal rate of a charge pulse solicitation to prevent this ageing has been developed. The approach relies on the use of a fundamental model of lithium-ion battery. The method was first assessed using Smith and Wang's data set of parameters. In a second time parameters for VL41M SAFT cell were considered in the theoretical approach. From these considerations the abacus, giving the highest current density to be applied versus SOC, could be set up.

For validation of the above method, 2 s microcycles were performed on this mass production SAFT cell. The relative capacity loss, attributed to Li plating, was evaluated thanks to the differentiation

$dV_{cell}/dSOC$ technique. The obtained experimental results are consistent with simulation abacus and theoretical curves. This approach can orient further specifications for suitable use of the battery as well as for electrode design. It must be noticed that the abacuses shown are only illustrations of the methodology: for other cells, new abacuses have to be set up according to their design, their physicochemical features and the electrical appliances used.

Acknowledgements

This work for PhD is financially supported by the French Association Nationale de la Recherche et de la Technologie (ANRT).

References

[1] M. Broussely, P. Biensan, F. Bonhomme, Ph. Blanchard, S. Herreyre, K. Nechev, R.J. Staniewicz, Journal of Power Sources 146 (2005) 90–96.
[2] M. Broussely, S. Herreyre, P. Biensan, P. Kasztejna, K. Nechev, R.J. Staniewicz, Journal of Power Sources 97–98 (2001) 13–21.
[3] G. Sarre, Ph. Blanchard, M. Broussely, Journal of Power Sources 127 (2004) 65–71.
[4] S. Bourlot, P. Blanchard, S. Robert, Journal of Power Sources 196 (2011) 6841–6846.
[5] J. Vetter, P. Novák, M. Wagner, C. Veit, K.-C. Möller, J. Besenhard, M. Winter, M. Wohlfahrt-Mehrens, C. Vogler, A. Hammouche, Journal of Power Sources 147 (2005) 269–281.
[6] P. Verma, P. Maire, P. Novák, Electrochimica Acta 55 (2010) 6332–6341.
[7] D. Aurbach, A. Zaban, Y. Ein-Eli, I. Weissman, O. Chusid, B. Markovsky, M. Levi, E. Levi, A. Schechter, E. Granot, Journal of Power Sources 68 (1997) 91–98.
[8] D. Aurbach, B. Markovsky, G. Salitra, E. Markevich, Y. Talyossef, M. Koltypin, L. Nazar, B. Ellis, D. Kovacheva, Journal of Power Sources 165 (2007) 491–499.
[9] S. Zhang, K. Xu, T.R. Jow, Journal of Power Sources 160 (2006) 1349–1354.
[10] S.S. Zhang, Journal of Power Sources 161 (2006) 1385–1391.
[11] P. Thounthong, S. Raël, B. Davat, Transactions on Energy Conversion 23 (2008) 148–155.
[12] P. Thounthong, S. Raël, B. Davat, Journal of Power Sources 193 (2009) 376–385.
[13] P. Arora, M. Doyle, R. White, Journal of the Electrochemical Society 146 (1999) 3543–3553.
[14] R.D. Perkins, A.V. Randall, X. Zhang, G.L. Plett, Journal of Power Sources 209 (2012) 318–325.
[15] K. Smith, C.-Y. Wang, Journal of Power Sources 160 (2006) 662–673.
[16] J. Newman, K.E. Thomas-Alyea, Electrochemical Systems, third ed., Wiley Inter-Science, 2004.
[17] M. Doyle, T.F. Fuller, J. Newman, Journal of the Electrochemical Society 140 (1993) 1526–1533.
[18] T.F. Fuller, M. Doyle, J. Newman, Journal of the Electrochemical Society 141 (1994) 1–9.
[19] M. Doyle, J. Newman, Electrochimica Acta 40 (1995) 2191–2196.
[20] M.W. Verbrugge, B.J. Koch, Journal of Electroanalytical Chemistry 436 (1997) 1–7.
[21] K. Smith, C.-Y. Wang, Journal of Power Sources 161 (2006) 628–639.
[22] K.A. Smith, C.D. Rahn, C.-Y. Wang, Energy Conversion and Management 48 (2007) 2565–2578.
[23] A.M. Colclasure, R.J. Kee, Electrochimica Acta 55 (2010) 8960–8973.
[24] S. Raël, M. Hinaje, Journal of Power Sources 222 (2013) 112–122.
[25] I.V. Thorat, D.E. Stephenson, N.A. Zacharias, K. Zaghib, J.N. Harb, D.R. Wheeler, Journal of Power Sources 188 (2009) 592–600.
[26] SAFT Communication Department, doc. n° 54042-2-0305, March 2005. http://www.saftbatteries.com/doc/Documents/liion/Cube572/54042_VLM_cells_0305.d0d8d859-9174-42f2-84b2-19632e4b0760.pdf (accessed 14.03.13).
[27] P. Liu, J. Wang, J. Hicks-Garner, E. Sherman, S. Soukiazian, M. Verbrugge, H. Tataria, J. Musser, P. Finamore, Journal of the Electrochemical Society 157 (2010) A499–A507.

Nomenclature

Symbols
a_{Li^+}: lithium ion activity
a_s: specific interfacial area on active particles ($m^2\ m^{-3}$)
c_e: concentration of salt ions (mol m^{-3})
c_s: concentration of inserted lithium in active solid material (mol m^{-3})
$c_{s,x}$: concentration of inserted lithium at the x abscise (mol m^{-3})
$c_{s,max}$: maximal concentration of inserted lithium (mol m^{-3})
C/n: charge or discharge rated capacity in n hours
D_e: diffusion coefficient of Li^+ in the solution ($m^2\ s^{-1}$)
D_s: diffusion coefficient of lithium inserted in the active particle ($m^2\ s^{-1}$)
E_a: activation energy (J mol^{-1})
E: potential of the electrode at the local Li^+ concentration (V vs Li^+/Li°)
E°: standard potential (V)
$f_\pm$: activity coefficient of salt
F: Faraday's constant (C mol^{-1})
J_{cell}: applied current density (A m^{-2})
j_0: exchange current density (A m^{-2})
j_{BV}: reaction current density resulting from production or consumption of lithium (A m^{-3})
$j_{ch,lim}$: limit charge current density to avoid Li plating (A m^{-2})
l: perpendicular axis to the electrode surface (m)
L: thickness (m)
OCV: open-circuit potential (V)
Q: capacity (A h)
r: perpendicular axis to the active particle surface (m)
R: gas constant (J $mol^{-1}\ K^{-1}$)
R_s: radius of solid particles (m)
t: time (s)
t_p: transference number of Li^+ ions
t_n: transference number of PF_6^- ions
T: temperature (K)
U: "apparent" equilibrium potential (V)
V: voltage (V)
x: dimensionless perpendicular axis to the electrode surface
x_{neg}: lithium stoichiometry in $Li_{x_{neg}}C_6$, defined as: $c_s\ c_s^{-1}{}_{,max}$ in the negative solid active particle
x_{pos}: lithium stoichiometry in $Li_{x_{pos}}Ni_{1-y-z}Co_yAl_zO_2$, defined as: $c_s\ c_s^{-1}{}_{,max}$ in the positive solid active particle
y: dimensionless perpendicular axis to the particle surface

Greek letters:
α_o, α_r: oxidation and reduction transfer coefficients
β: Bruggeman exponent coefficient
Δt_{rest}: time duration of rest periods (s)
Δt_{ch}: time duration of charge period (s)
Δt_{dch}: time duration of discharge period (s)
ε_e: porosity of electrode or separator
ε_s: volume fraction of solid active material
δ, ε: stoichiometric coefficients
η: overpotential (V)
κ_e: electrolyte ionic conductivity (S m^{-1})
κ_s: composite electrode electronic conductivity (S m^{-1})
σ_s: electrode electronic conductivity (S m^{-1})
τ: tortuosity
Φ_e: solution phase potential (V)
Φ_s: solid active particle potential (V)

Subscripts:
cell: relative to the cell
e: electrolyte solution phase
eff: effective
e^-: electron
Li: lithium inserted specie
Li°: lithium metal
Li^+ or +: lithium ion in electrolyte
lim: limit value
PF_6^- or −: salt anion
n or neg: negative electrode domain
max: maximal
mean: mean value
p or pos: positive electrode domain
s: separator or solid phase or surface
theo: theoretical

Acronyms
CTL: charge transfer limitation
DMC: dimethyl carbonate
EC: ethylene carbonate
$LiPF_6$: lithium hexafluorophosphate
PC: propylene carbonate
SEI: solid electrolyte interphase
SDL: solid diffusion limitation
SOC: state of charge